Monitoring temperature in high enthalpy arc-heated plasma flows using tunable diode laser absorption spectroscopy

Marcel Nations Martin[1], Leyen S. Chang[2], Jay B. Jeffries[3], and Ronald K. Hanson[4]
Stanford University, Stanford, California 94305-3032

Anuscheh Nawaz[5], Jaswinder S. Taunk[6], David M. Driver[7], and George Raiche[8]
NASA Ames Research Center, Moffett Field, California 94035

A tunable diode laser sensor was designed for *in situ* monitoring of temperature in the arc heater of the NASA Ames IHF arcjet facility (60 MW). An external cavity diode laser was used to generate light at 777.2 nm and laser absorption used to monitor the population of electronically excited oxygen atoms in an air plasma flow. Under the assumption of thermochemical equilibrium, time-resolved temperature measurements were obtained on four lines-of-sight, which enabled evaluation of the temperature uniformity in the plasma column for different arcjet operating conditions.

Nomenclature

e	=	electron charge
ε_0	=	emissivity
m_e	=	electron mass
c	=	speed of light
k_B	=	Boltzmann constant
h	=	Planck constant
$\hbar$	=	Reduced Planck constant
λ	=	wavelength
v	=	frequency
ϕ	=	lineshape
Γ	=	Gamma Function
$V(a, w)$	=	Voigt Function
L	=	optical pathlength
Q	=	partition function
T_e	=	electron temperature
T_{ex}	=	excitation temperature
ECDL	=	external cavity diode laser
TPS	=	thermal protection system
TDLAS	=	tunable diode laser absorption spectroscopy
MLOS	=	multiple lines-of-sight
IHF	=	Interaction Heating Facility
CEA	=	Chemical Equilibrium with Applications

---

[1] Graduate Research Assistant, High Temperature Gasdynamics Laboratory, Dept. of Mechanical Eng.
[2] Graduate Research Assistant, High Temperature Gasdynamics Laboratory, Dept. of Mechanical Eng.
[3] Senior Research Associate, High Temperature Gasdynamics Laboratory, Dept. of Mechanical Eng., Associate Fellow AIAA.
[4] Professor, High Temperature Gasdynamics Laboratory, Dept. of Mechanical Eng., Fellow AIAA.
[5] Senior Aerospace Engineer, Sierra Lobo Inc., NASA Ames Thermophysics Facilities Branch, Member AIAA.
[6] Senior Research Engineer, Jacobs Technology, NASA Ames Thermophysics Facilities Branch, Member AIAA.
[7] Research Scientist, NASA Ames Thermophysics Facilities Branch, Member AIAA.
[8] Branch Chief, NASA Ames Thermophysics Facilities Branch, Member AIAA.

I. Introduction

THE next generation of hypersonic vehicles needed to support the International Space Station drives the ongoing development of a new class of non-ablative, high temperature materials to enable the high lift-to-drag ratio vehicle concepts designed for efficient, regular transport.[1] Novel new thermal protection systems (TPS) are also required for the new generation of smaller-scale planetary probes that are designed to return information and eventually local samples from potentially life-sustaining environments within the solar system.[2] Current vehicle concepts envision a fraction of the total weight (12-70 %) of returning planetary probes to be devoted to heat shield, where a substantial portion of this TPS weight is uncertainty margin.[2] Thus, reduced uncertainty in the performance of TPS has the potential for significant improvement in the payload capability of interplanetary return vehicles.

The high-power (60 MW), large-scale Interaction Heating arcjet Facility (IHF) at NASA Ames Research Center has been a reliable source of high-enthalpy gas (5000-8000 K, 2-9 atm) used to simulate reentry aerothermal environments and test new materials for TPS.[3] Currently, arcjet test conditions are defined using either the expected heat-flux level or the anticipated surface temperature for a particular material in its envisioned application.[3] While this is sufficient to evaluate relative performance levels, it is not sufficient for establishing absolute capability for materials or for integrated TPS. This lack of traceability of the TPS test environment to the actual vehicle performance environment significantly increases the margin of TPS uncertainty. Optimization of TPS safety margins, however, requires well-understood gas stream conditions that can be accurately predicted by numerical models and with known temporal fluctuations.

The IHF operates in a high temperature regime, where almost all of the molecular oxygen present in the heated air flow is dissociated into oxygen atoms. The spectrum of atomic oxygen at high temperatures is comprised of several strong electronic transitions and the populations of the excited electronic states are extremely temperature sensitive. In this study, the population in the $3s^5S^0_2$ excited level of atomic oxygen is monitored by absorption of laser light near 777.2 nm and, by assuming the plasma to be in local thermodynamic equilibrium (LTE), temperature can be inferred from the composition of the input flow (air and argon) coupled with a facility measured pressure.[4]

Previous studies of the IHF arc-heated plenum via emission spectroscopy pointed to the existence of both spatial and temporal nonuniformities within the plasma.[5] It has been suggested that short time-scale fluctuations were related to the complex mixing process caused by significant radial injection of cold air adjacent to the measurement location.[5] In addition, it is speculated that a slow swirl (< 0.1Hz) of the arc-attachment, due to a current-induced magnetic field in the heater, promotes long time-scale fluctuations in the plenum during the course of a test run. Hence, to gauge the degree of nonuniformity in the plenum chamber, an external cavity diode laser (ECDL) sensor was developed for *in situ* concurrent measurements of arc-heated gas temperature at multiple lines-of-sight (MLOS).

II. Theory

The energy diagram of a few relevant electronic transitions of atomic oxygen is shown in Fig. (1). The lower state of the oxygen transition at 777.2 nm is a metastable state, that is, it is not coupled to the ground state via one-photon selection rules. At elevated temperatures, the population in this state increases to measurable levels, and the transition can have strong absorption intensity. Important parameters for the $O(^5P_3 \leftarrow ^5S^0_2)$ transition such as line center wavelength (λ_o), Einstein coefficient (A_{ul}), oscillator strength (f_{lu}), upper state energy (E_u), upper state degeneracy (g_u), lower state energy (E_l), and lower state degeneracy (g_l) are shown in Table 1 below.[6]

Table 1. Fundamental spectroscopic data for the $O(^5P_3 \leftarrow ^5S^0_2)$ transition.

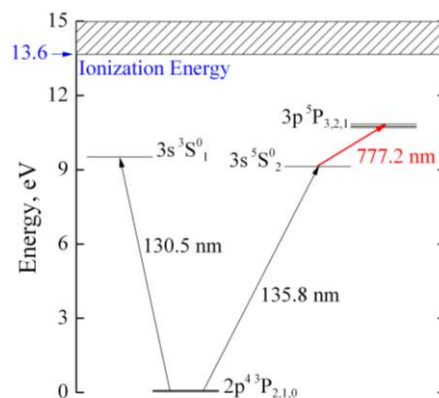| Atom	λ_o (nm)	A_{ul} (10^6 s^{-1})	f_{lu}	E_l (cm^{-1})	E_u (cm^{-1})	g_l	g_u
Oxygen	777.2	36.9	0.468	73768	86631	5	7

Figure 1. Illustrative energy-level diagram of atomic oxygen.

A. TDLAS for Plasma Diagnostics

Tunable diode laser absorption spectroscopy (TDLAS) is a powerful, non-intrusive optical diagnostics technique that has been widely used for sensing gas species in a variety of harsh environments.[7,8] For air plasma diagnostics, TDLAS is particularly attractive since strong isolated electronic transitions of excited O, N, and Ar atoms exist in the visible and near-infrared (NIR) regions of the spectrum where diode lasers are readily available. In addition, diode laser based sensors are compact, rugged, and can be easily fiber-coupled for remote operation.

When the diode laser linewidth is narrow compared to absorption linewidth, the light source may be treated as monochromatic. As the laser beam propagates through a linearly absorbing medium, the beam intensity will decrease exponentially according to the Beer-Lambert relation:

$$\left(\frac{I}{I_0}\right)_v = \exp(-\alpha_v) = \exp(-S_{lu}^* n_l \phi_v L) \tag{1}$$

where

$$S_{lu} = \frac{\lambda_o^2}{8\pi c} A_{ul} \frac{g_u}{g_l}\left[1 - \exp\left(-\frac{hc}{\lambda_o k_B T_{ex}}\right)\right] \tag{2}$$

Here, $(I/I_o)_v$ is the spectral transmittance, α_v is the spectral absorbance, S_{lu} (cm^{-1}/(molecule·cm^{-2})) is the linestrength of the transition, n_l (cm^{-3}) is the lower state number density, ϕ_v is the lineshape function, L is the optical pathlength, k_B is the Boltzmann constant, c is the speed of light, and T_{ex} is the excitation temperature that describes the ratio of populations in the lower and upper states of the transition. The integrated area of absorbance is obtained by fitting the absorption lineshape to a Voigt profile and it can be calculated by taking the frequency integral of the spectral absorbance in Eq. (1):

$$A_{int} = \int_v \alpha_v dv = S_{lu}^* n_l L \qquad \text{where} \qquad \int_v \phi_v dv = 1 \tag{3}$$

The exponential term in Eq. (2) is relatively insensitive to changes in T_{ex}, and can be neglected in most cases, owing to the smallness of the term. In this study we make equilibrium assumptions with regard to the thermodynamic state of the heated gas, which allow for the determination of a common temperature from the number density in the lower excited state, n_l, measured using Eq. (3).

B. Plasma Thermodynamic State at the IHF Arc Heater

Given the elevated temperatures in the IHF arc heater, the plasma was modeled as a 13-species (O_2, N_2, NO, O, N, Ar, O_2^+, N_2^+, NO^+, O^+, N^+, Ar^+, and e$^-$) gas mixture. Thus, in order to fully characterize the thermodynamic state of the air plasma, one shall consider the following assumptions:

1. Thermal Equilibrium

The arc heater operates at high pressures where the rates of collisional excitation and de-excitation by electron impact are high compared to depleting radiative rates. As a result, the relative populations of all electronic levels can be assumed to follow a Boltzmann distribution described by a common temperature.

2. Chemical Equilibrium

In order to calculate the total number density of each species in the plasma flow, one must resort to assumptions of chemical equilibrium. According to collision theory, chemical reactions occur when particles collide at specific orientations and with sufficient energy to break or form bonds. As temperature and pressure increases, the likelihood that a collision will result in a reaction increases, and so does the rate at which chemical equilibrium is reached. Given the high temperatures and pressures in the plenum, we assume that chemical equilibrium is reached by the time the hot gas arrives at the measurement location.

3. Local Thermodynamic Equilibrium Plasma

Plasma is said to be in local thermodynamic equilibrium if both thermal and chemical equilibrium assumptions hold. In this case, the gas can be described by a common temperature T. Previous measurements on excited oxygen and nitrogen atoms in the arc heater yielded the same gas temperature demonstrating that the assumption of local thermodynamic equilibrium is applicable in the arcjet heater.[4]

C. Path-Averaged LTE Temperature Measurements

For LTE plasma, the lower state number density of an electronic transition can be related to the total number density of the absorbing oxygen atoms, by the following equation:

$$\frac{n_l}{n_o} = \frac{g_l}{Q_o} \exp\left(-\frac{E_l}{k_B T}\right) = B(T) \tag{4}$$

where B is the Boltzmann fraction, n_O is the total atomic oxygen number density and Q_O is the atomic oxygen partition function. Theoretically, the partition function can be written in terms of the contribution from all energy levels as follows:

$$Q_o = \sum_{j}^{\infty} g_j \exp\left(-\frac{E_j}{k_B T}\right) \tag{5}$$

In this study, the electronic partition function of atomic oxygen is modeled using the few-level approach described by Colonna.[9] All the atomic levels are grouped into a few lumped levels with suitable average energy ε and global statistical weight G, dependent only on the energy cutoff criterion selected to lower the ionization potential used to truncate the partition function. Thus, Q_O is given by the following equation with T expressed in eV:[9]

$$Q_o = 9 \exp\left(-\frac{0.00967077}{T}\right) + 6 \exp\left(-\frac{2.33774}{T}\right) + G \exp\left(-\frac{\varepsilon}{T}\right) \tag{6}$$

Tabulated values of G and ε are shown in Table 2 for a few ionization cutoff energies, Δ_s.[9] The partition function is plotted in Fig. (2) as a function of temperature. Given the temperature range of interest (5000-8000 K), Q_O is nearly independent of the tabulated cutoff energies, and thus the smallest value of $\Delta_s = 250$ cm^{-1} was chosen.
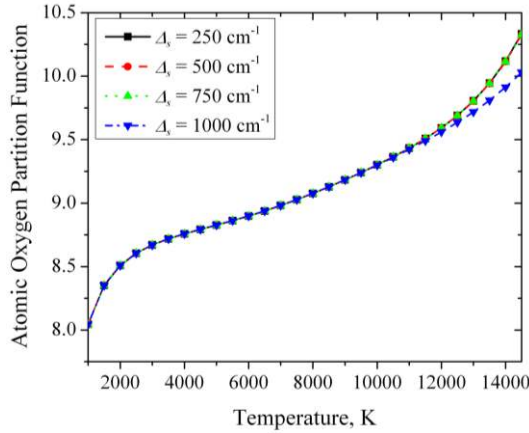

Table 2. Number of levels and group data as a function of the ionization cutoff energy for O atoms

Δ_s (cm^{-1})	Number of Levels	G	e (eV)
250	94	22,940	13.4656
500	83	22,660	13.4643
750	79	22,564	13.4639
1000	68	7844	13.3727

Figure 2. Polynomial fit of the electron impact parameter as a function of electron temperature.

The total number density of atomic oxygen in Eq. (4) is determined from the equation of state. For plasmas, the ideal gas law must be modified in order to account for long range Coulomb forces since charge neutrality is not satisfied within the Debye length λ_D.[10] However, the IHF arc-heated plasma is weakly ionized, and the number density of electrons is $n_e \sim 10^{15}$-10^{16} cm^{-3}. Consequently, the arc-heated plasma may be modeled as an ideal gas, and the equation of state is simply given as: [10]

$$P = n k_B T - \frac{k_B T}{24 \pi \lambda_D^3} \approx n k_B T \tag{7}$$

Therefore, from Dalton's Law of partial pressures, it follows:

$$n_o = \frac{PX_o}{k_B T} \tag{8}$$

where X_O is the mole fraction of atomic oxygen. Since chemical equilibrium is assumed, n_o can be determined as a function of the translational temperature for a given pressure. Note that pressure is assumed constant across the plasma column. NASA's program Chemical Equilibrium with Applications (CEA)[11] can predict high temperature air composition at specified temperature and pressure up to 20000 K. Equilibrium mole fractions for neutral and charged plasma species are shown in Fig. (3) for a typical mixture of 7.5% Ar in dry air at the limit arcjet pressures of 2 atm and 9 atm.

Finally, a path-averaged LTE temperature T is calculated iteratively using Eqs. (3) and (4).

a)

b)
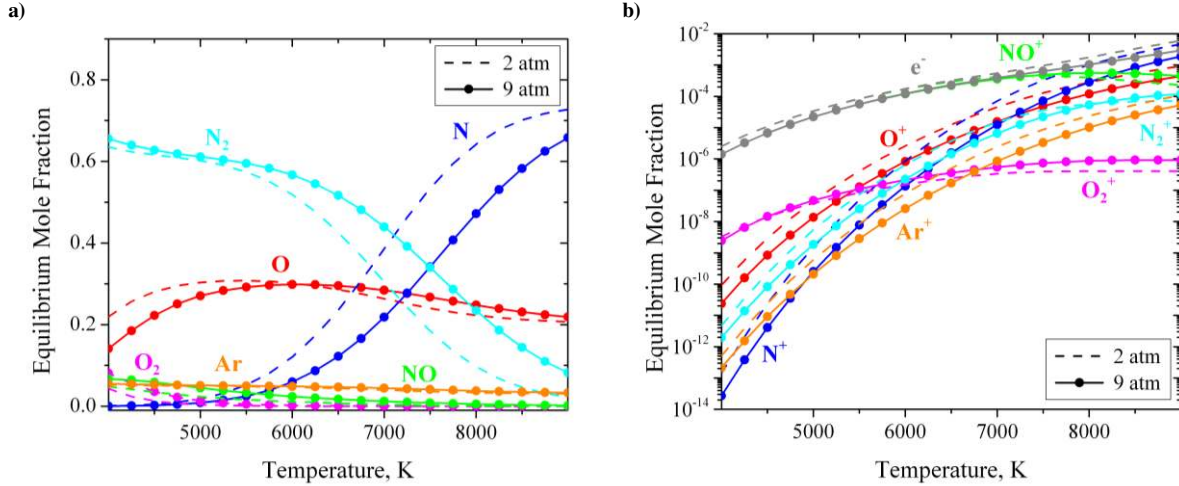
Figure 3. **Chemical equilibrium analysis using NASA CEA software for a 13-species air model at the limiting arc heater pressures of 2 atm and 9 atm. The plots above show the variability of equilibrium mole fractions for a) neutral species and b) charged species.**

In order to illustrate the high temperature sensitivity of the measurement scheme, the Boltzmann fraction in Eq. (4) is plotted versus temperature in Fig. (4). Note that the fraction of the oxygen atoms in the $^5S^0_2$ state increases by more than an order-of-magnitude for every increase of 1000 K in temperature.
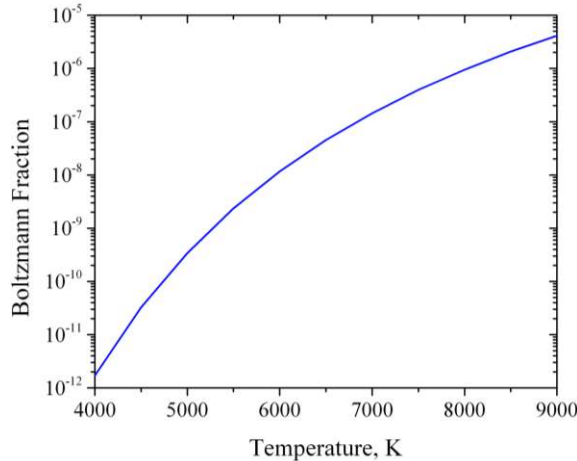
Figure 4. **Boltzmann fraction of atomic oxygen in $^5S^0_2$ state.**

D. Plasma Line Broadening Mechanisms

Broadening of an absorption feature occurs due to various physical mechanisms that perturb transition's energy levels or the way light interacts with individual gas species in the medium. For the air plasma, the lineshape of the metastable oxygen transition at 777.2 nm can be determined by Gaussian (Doppler, instrumental) and Lorentzian

American Institute of Aeronautics and Astronautics

(van der Waals, Stark, natural, resonance) broadening effects, where a convolution of both constituent distributions result in a Voigt profile. In order to accurately model the absorption profile for a given arcjet operating condition, it is important that contributions from each broadening mechanism are properly accounted for.[12] In the IHF, effects of natural, resonance, and instrumental broadening of the 777.2nm feature are insignificant, and are neglected here. Note the laser linewidth (≤ 300 kHz) is less than 10^{-5} of the absorption linewidth. The dominant mechanisms are Doppler, van der Waals, and Stark broadening, and a brief description of these effects follows.

1. Doppler Broadening

The Doppler broadening is due to the thermal motions of the gas medium. When an absorbing particle travels with a velocity component in the same direction as the propagation of the laser beam, there will be a shift in the frequency at which this particle will absorb a photon (known as Doppler shift). Given that the random velocities of the absorbing species can be described by a Maxwellian distribution function, the lineshape function will have a Gaussian form; the Doppler full-width at half-maximum (FWHM) is related to the translational temperature according to the following equation:

$$\Delta\lambda_D = \lambda_o \sqrt{\frac{8k_B T \ln 2}{m_O c^2}} \tag{9}$$

2. Van der Waals Broadening

In plasmas, van der Waals broadening arises from the dipole interaction of an excited atom with the induced dipole of a neutral atom in the ground state via collisions. The resulting lineshape can be described by a Lorentzian profile with a FWHM given by the following expression by Griem[13] for an absorber *a* colliding with perturber *p*:

$$\Delta\lambda_{vdW} \approx \frac{\lambda_o^2}{c}\left(\frac{9\pi\hbar^5 \overline{R_\alpha^2}}{16m_e^3 E_p^2}\right)^{2/5} \overline{v_{ap}^{3/5}} n_p \tag{11}$$

Here, E_p, $\hbar$, m_e, v_{ap}, and n_p are the perturber resonance-level excitation energy, reduced Planck constant, electron mass, relative speed between absorber and perturber, and perturber number density, respectively. In the above expression, the square of the coordinate vector is:

$$\overline{R_\alpha^2} \approx \frac{1}{2}\frac{E_H}{E_\infty - E_\alpha}\left[5\frac{z^2 E_H}{E_\infty - E_\alpha} + 1 - 3l_\alpha\left(l_\alpha + 1\right)\right] = 44.5 \tag{12}$$

where E_∞ and E_H are the ionization potential of the absorber and the hydrogen atom, E_α is the excitation potential of the upper state of the transition, l_α is the orbital quantum number, and z is the number of effective charges.[14] In this case, for an atomic oxygen absorber $E_\infty = 13.614$eV, $E_H = 13.6$eV, $E_\alpha = 10.75$eV, $l_\alpha = 1$ and $z = 1$.

In Eq. (11), the relative velocity term can be written in terms of the mean speed:

$$\overline{v_{ap}^{3/5}} = \left(\frac{4}{\pi}\right)^{2/10}\Gamma\left(\frac{9}{5}\right)\left(\overline{v_{ap}}\right)^{3/5} \cong 0.98\left(\overline{v_{ap}}\right)^{3/5} = 0.98\left(\frac{8k_B T}{\pi m_{ap}^*}\right)^{3/5} \tag{13}$$

Here, m_{ap}^* is the reduced mass of the absorber and the perturber. According to Fig. (3), for the operating conditions of the IHF (5000-8000 K, 2-9 atm), the plasma in the arc heater is weakly ionized and mainly composed of neutrals. Therefore, a summation is carried over all major perturbers in the plasma and Eq. (11) can be rewritten as:

$$\Delta\lambda_{vdW} \approx 0.98\frac{\lambda_o^2}{c}\left(\frac{9\pi\hbar^5 \overline{R_\alpha^2}}{16m_e^3}\right)^{2/5}\left(\frac{8k_B T}{\pi}\right)^{3/10}\frac{P}{k_B T}\sum_p\left[\frac{X_p}{E_p^{4/5}\left(m_{ap}^*\right)^{3/5}}\right] \tag{14}$$

In the above equation, X_p is the mole fraction of the perturber p. The values of m_{ap}^* and E_p for the major air plasma species are listed in Table 3 below.[14]

Table 3. Van der Waals perturber constants for an atomic oxygen absorber

Perturber	m^{*}_{ap} (10⁻²⁶ kg)	E_p (10⁻¹⁸ J)
O	1.33	1.52
N	1.24	1.65
O_2	1.77	0.99
N_2	1.69	2.02
NO	1.73	0.88
Ar	1.90	1.86

3. Stark Broadening

Coulombic interactions between the absorbers outer electrons and the charged particles in the plasma (electrons and ions) lead to broadening of the feature. For non-hydrogenic species, the theoretical Stark broadening width (FWHM) $\Delta\lambda_S$ (Å) can be described by the following equation:[15]

$$\Delta\lambda_S = 2\left[1+1.75\times10^{-4}\,n_e^{1/4}\alpha\left(1-0.068n_e^{1/6}T_e^{-1/2}\right)\right]\left(\frac{n_e}{10^{-16}}\right)w$$

(15)

where n_e (cm⁻³) is the number density of free electrons and T_e is the electron temperature. The electron impact parameter w (Å) and the ion broadening parameter α are obtained from tabulated values by Griem,[16] and fitted with a polynomial and exponential decay function, respectively. Both parameters are plotted in Fig. (5) as a function of electron temperature for atomic oxygen.
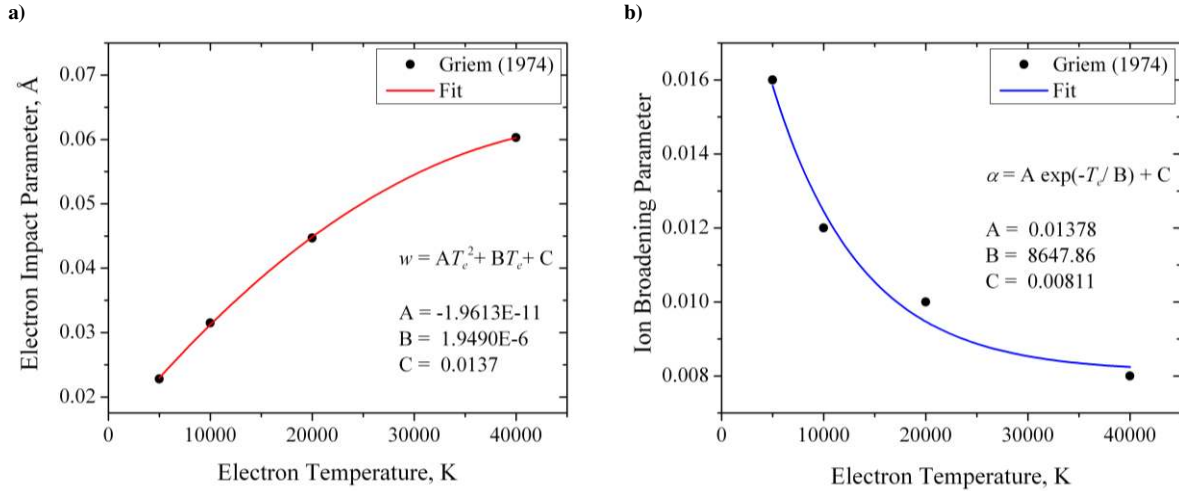
a)

b)

$\alpha = A\,exp(-T_e/B) + C$

A = 0.01378
B = 8647.86
C = 0.00811

$w = A\,T_e^2 + B\,T_e + C$

A = -1.9613E-11
B = 1.9490E-6
C = 0.0137

Figure 5. **a) Polynomial fit of the electron impact parameter *w* as a function of electron temperature. b) Exponential decay fit of the ion broadening parameter *α* as a function of electron temperature.**

The total Gaussian and Lorentzian broadening widths of the transition can be calculated by summing the contributions from each of the individual broadening mechanisms described above. The total Gaussian FHWM is:

$$\Delta\lambda_G \approx \Delta\lambda_D$$

(17)

and the total Lorentzian FWHM is:

$$\Delta\lambda_L \approx \Delta\lambda_{vdW} + \Delta\lambda_S$$

(18)

These parameters will vary according to the conditions at which the IHF is operating. In Fig. (6) below, the FWHM widths are plotted as a function of temperature, for the two limiting pressure cases assuming a mixture of 7.5% Ar in dry air. In the low pressure regime, Doppler and van der Waals broadening are dominant when temperatures are below ~6000 K, but as temperature increases the contribution from Stark broadening also increases. In the higher pressure regime, Doppler broadening remains constant since it does not depend on pressure, and the van der Waals broadening is dominant. Like in the lower pressure scenario, Stark broadening is more significant at higher temperatures.
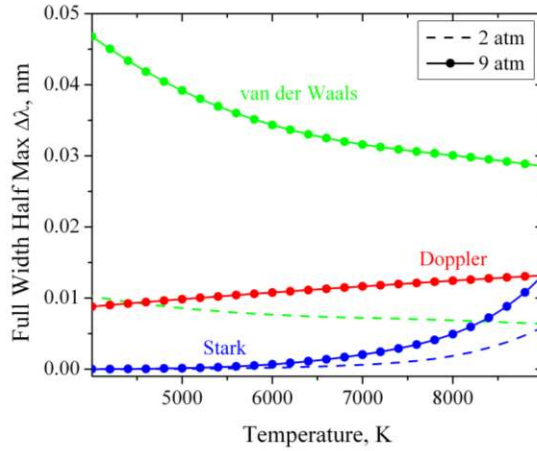
Figure 6. Broadening widths (FWHM) for the atomic oxygen transition at 777.2 nm.

E. Lineshape Function: Voigt Profile

The Doppler and collisional broadening mechanisms discussed above are decoupled, and neither can be neglected for the conditions at which the IHF facility operates. Therefore, the appropriate lineshape to model the absorbance will be a convolution of a Gaussian and Lorentzian lineshapes known as Voigt lineshape:

$$\phi_V(v) = \int_{-\infty}^{\infty} \phi_G(u) + \phi_L(v-u) = \phi_D(v_o)\frac{a}{\pi}\int_{-\infty}^{\infty}\frac{\exp(-y^2)dy}{a^2+(w-y)^2} = \phi_D(v_o)V(a,w) \tag{19}$$

Here, w is the non-dimensional line position, $\phi_D(v_o)$ is the line center magnitude of the Doppler lineshape, and a is the so-called Voigt "a" parameter, which is defined as a ratio between the Lorentzian and Gaussian FWHM broadening coefficients:

$$a = \frac{\sqrt{\ln 2}\Delta\lambda_L}{\Delta\lambda_G}, \text{ and } \quad w = \frac{2\sqrt{\ln 2}(v-v_o)}{\Delta\lambda_G} \tag{20}$$

For a given measured absorption profile, the Voigt lineshape is fitted using the numerical approximation algorithm by Humlicek[17] and a value for the integrated area is directly obtained. Thus, a LTE temperature can be computed by following the steps described in the previous subsections. Figure (7) shows a plot of the integrated area as a function of temperature for a typical IHF input gas mixture of 7.5% Ar in dry air at different pressures.
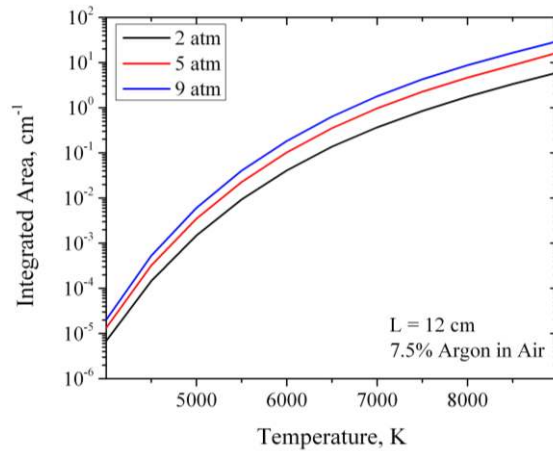

Figure 7. Integrated absorbance area vs. LTE temperature for an optical pathlength of 12 cm.

8
American Institute of Aeronautics and Astronautics

III.   Experimental Setup

A. Interaction Heating Facility: IHF

The 60 MW Interaction Heating arcjet Facility has the capability to generate high temperature hypersonic flows for several minutes, which simulate reentry aerothermal environments suitable for ground test of TPS,[3] as shown in Fig. (8). The IHF arc heater consists of two sets of electrodes, separated by a constrictor tube made of multiple stacked water-cooled copper disks.[3] To ensure easy start of the arc and sufficient ionization in the vicinity of the electrodes, argon gas is used to sheath each electrode disk.[10] Test gas (usually air) is radially injected into the constrictor tube and heated by an electric arc attached between the electrodes. Free electrons, accelerated by an applied electric field, transfer kinetic energy to heavy particles through collisions thereby heating the gas. Typically, the arc heater operates at pressures of 2-9 atm and temperatures of 5000-8000 K.[3] The hot, high pressure plasma expands through a convergent-divergent nozzle and flows into an evacuated chamber at hypersonic speeds (5-10 km/s) over a test article positioned downstream of the nozzle exit. A schematic of the IHF arcjet is shown in Fig. (9).

Figure 8. Top view of the IHF test cabin during a TPS test run.

At the IHF arc heater, for certain run conditions, a significant amount of room temperature air is transversely injected upstream from the nozzle inlet in order to tailor the flow enthalpy to desired conditions (henceforth, we shall refer to this as "add-air" injection). The add-air mixes with the hot gas, rapidly cooling the arc-heated stream and lowering its bulk enthalpy. Due to high heater pressures, the rate of particle collisions is relatively high, and the plasma is expected to reach equilibrium prior to entering the nozzle. However, the add-air disrupts the chemical equilibrium condition of the flow and for runs at the lower pressure regime, with significant add-air injection, mixing with the working fluid may not be complete.

In addition, in order to reduce copper erosion at the electrode surface due to thermal loads caused by the attached electric arc, a current-induced magnetic field is used to spin the arc-attachment and minimize local heating.[10] A reduction in electrode erosion means less flow contamination as well as reduced facility downtime for maintenance.

Both the add-air mixing process and the arc-attachment swirl are not well understood phenomena. There is still significant amount of uncertainty as to how these two processes affect the thermal field of the plasma, and their relative contributions to flow nonuniformities in the arc heater. In order to further investigate these processes, an experimental study was conducted using laser absorption techniques to optically probe the cross-section of the arc heater, adjacent to the nozzle inlet, at multiple lines-of-sight.
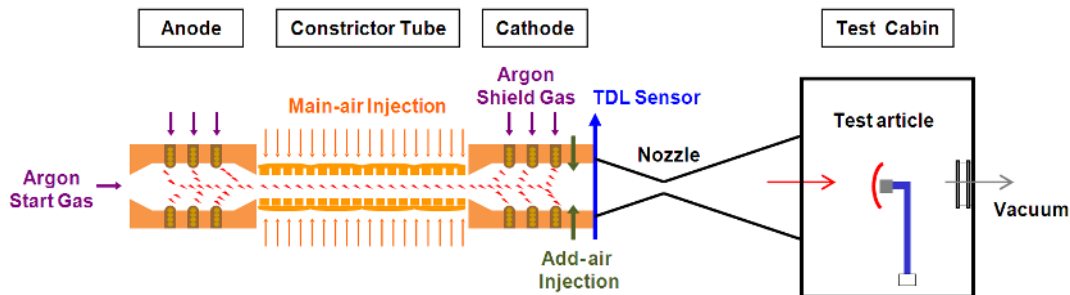

Figure 9.   Schematic of the IHF arcjet. TDLAS experiments at multiple lines-of-sight are carried upstream from the nozzle inlet.

B. Optical Disk

Figure (10) shows a copper segment from the arc heater modified to mount several optical telescope assemblies and direct laser light across the column of gases. There is some concern that a significant radial gradient in gas temperature exists in the arc-heated gases, thus the optical disk was designed to allow for simultaneous diagnostics at four different optical ports. Port B (L = 12.0 cm) corresponds to the cross-section centerline, ports A and C (L = 10.8 cm) are symmetric with respect to the centerline, and port D (L = 6.5 cm) investigates gases near the wall.

American Institute of Aeronautics and Astronautics

Since the test gas is heated by high-current, high-voltage arcs, any instrumentation on the arc heater or nozzle expansion must be electrically isolated. In addition, physical access to the optical disk is severely limited by a multitude of cooling lines and by the close proximity of the optical disk to the nozzle base plate. Therefore, fiber-coupled optical strategies are ideally suited for remote sensing at the IHF. Figure (11) shows the optical disk assembled in the cathode electrode package. Note the very short path between the optical disk and add-air injection.
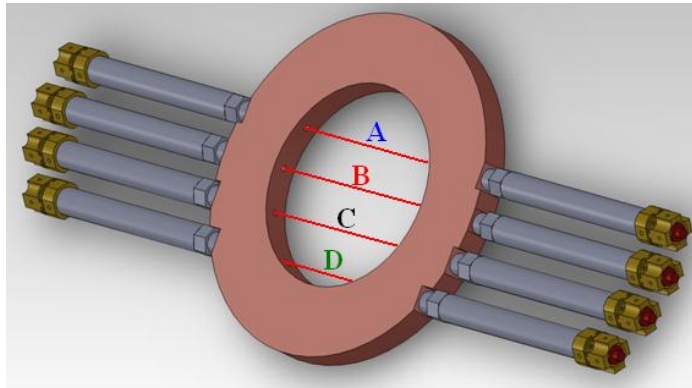
Figure 10.   Arc heater optical disk, designed to mount multiple telescope assemblies and direct laser light across the column of hot gases.
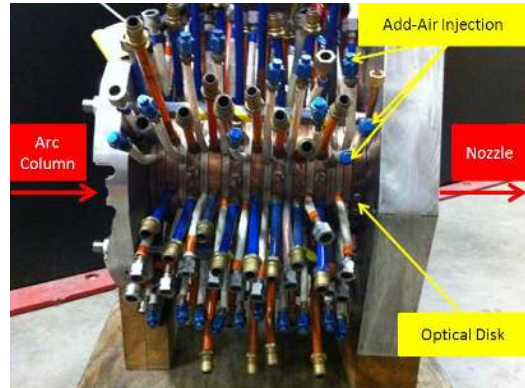
Figure 11.   Assembled cathode electrode package containing optical disk and add-air disks.

C.   External Cavity Diode Laser Sensor

Laser light from a New Focus Vortex II ECDL (~50mW) is fiber-coupled into a single-mode optical fiber, with 40% coupling efficiency. The effective laser power output (~20mW) is then split four ways by a fiber-coupled beam-splitter and laser light is routed to the arcjet using four polarization-maintaining, single-mode optical fibers (PM780-HP, 5μm core diameter, 0.13 numerical aperture (NA)). At the measurement location, laser beams are collimated using fiber-coupled aspheric lens collimators. Each beam is collimated using an 8.00 mm focal length, 0.50 NA fiber-coupled lens collimator with an approximate output beam diameter of ~1.5 mm. Each collimator is fixed to an alignment fixture with pointing and translation adjustment for optimization of signal throughput. The laser beams are pitched into free space and directed across the hot gas in the arc heater with specially designed telescopes housing small, AR-coated fused silica optical windows. A schematic of the optical telescope is shown in Fig. (12). After the light beams pass through the column of gas, they are collected with a second set of telescope assemblies and focused onto multimode fibers (400μm core diameter, 0.48 NA). The laser beams exiting the fibers are then focused onto switchable gain, silicon detectors with narrow band-pass filters to reduce emission noise (center frequency: 780±2 nm, FWHM: 10 ± 2 nm). The laser sensor was assembled in a single relay rack, which houses the laser head, laser controller, and a computer with a LabVIEW-based user interface to control laser output, collect absorption signals, perform data analysis and provide real-time temperature readout. The sensor rack is located ~15 m from the arc heater for operator access during the arcjet runs, as illustrated in Fig. (13).

Laser beam alignment is perhaps the most important procedure when setting up an experiment in the IHF. A properly aligned beam is critical for successful absorption measurements as it ensures reduced beamsteering noise caused by the interaction between laser light and the plasma, as well as minimal facility access time between runs for adjustments. The limited physical access due to the multiple cooling lines coupled with the lack of optical access to the inner section of the arc heater makes alignment in a mounted electrode package a cumbersome and time consuming task. Therefore, in order to ensure an optimized signal throughput, the disk is pre-aligned prior to electrode package assembly, and alignment is monitored throughout the assembly process, until the electrode is fully mounted on the arcjet. A full system checkup is performed before lighting the arc, during water and air leak tests, to ensure the signal baseline is steady and unaffected by mechanical vibrations and optical telescopes have good vacuum seal.
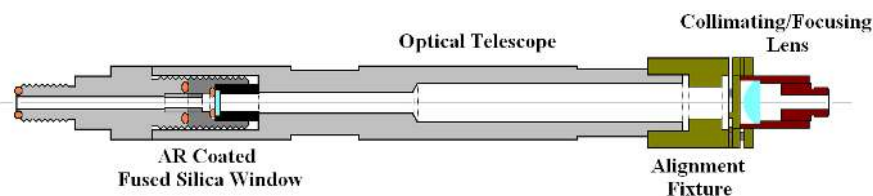

Figure 12.   Optical telescope and window assembly with fixture for adjustment of laser beam alignment.
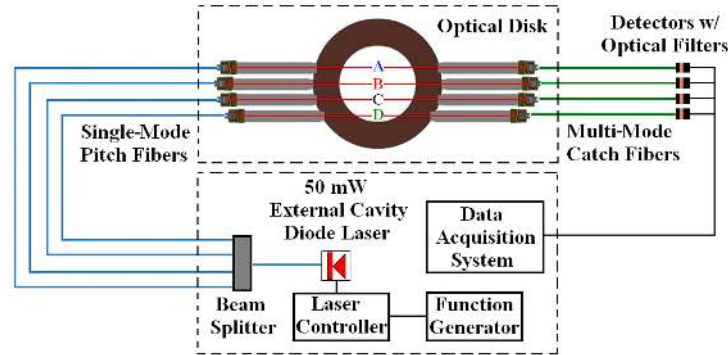
Figure 13.   Schematic of the TDL sensor setup at the IHF.

D. **Laser Sensor Validation: Microwave Plasma Discharge**

In order to validate laser scanning capabilities, laboratory tests of absorption sensing of the excited $^5S^0_2$ state of atomic oxygen were conducted using a discharge flow tube as illustrated in Fig. (14). A low pressure (0.5-4 Torr) flow of oxygen is directed through a 13mm diameter glass tube. A microwave discharge at 2.45 GHz is initiated in this flow in an Evenson cavity. The plasma dissociates a fraction of the molecular oxygen and the electron impact in the plasma produces a non-equilibrium distribution of electronic states in the atomic oxygen. This is in contrast with the arc heater which operates at high temperatures, pressures of several atmospheres, and is in LTE. The ends of the discharge tube are terminated with windows angled at Brewster's angle and the laser light is directed through a solid etalon (2.00 GHz free spectral range) and along the length of the tube. The laser is tuned in wavelength across the atomic oxygen absorption feature near 777.2 nm, and example absorption data are shown below in Fig. (15).
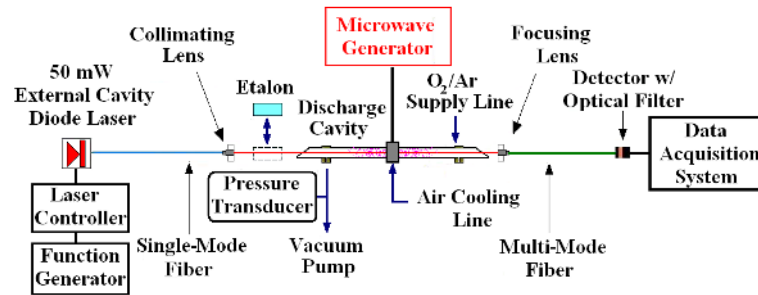

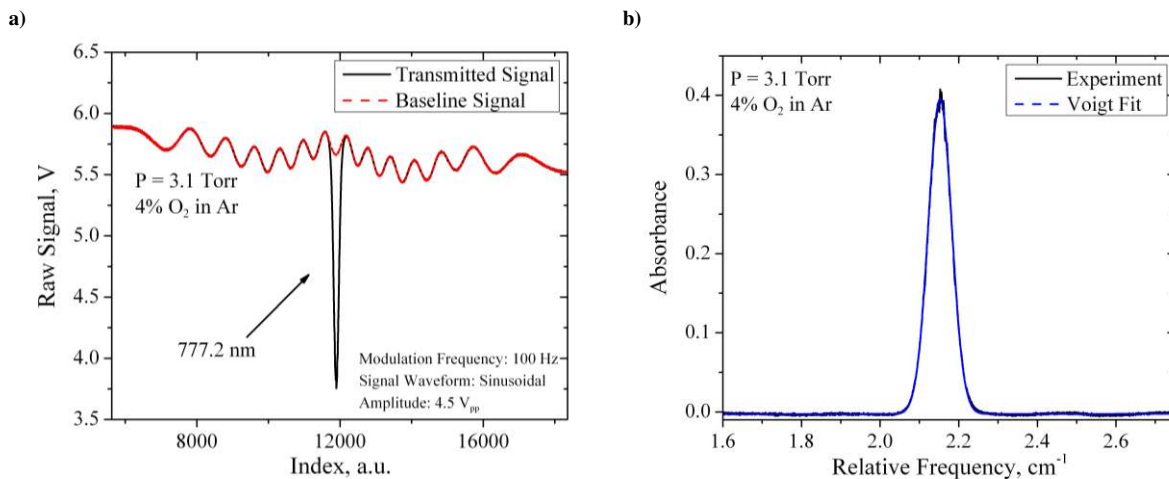Figure 14.   Setup for absorption measurements in a plasma discharge flow.

Figure 15. a) Example transmission data for atomic oxygen near 777.2 nm at 0.5 Torr. b) Absorption profile fit to a Voigt lineshape.

American Institute of Aeronautics and Astronautics

IV. Results & Discussion

Time-resolved, path-averaged LTE temperature measurements were made during several arcjet runs for different plasma bulk enthalpies and varying amounts of add-air injection. The results presented in this paper are the first multiple lines-of-sight (MLOS) measurements in the arc heater of the IHF using TDLAS. In addition, earlier single line-of-sight TDLAS measurements did not have sufficient signal-to-noise ratio (SNR) for successful measurements with significant cold air injection.[10] Thus, we present the first successful absorption measurements in the IHF arc heater at high add-air conditions.

Temperature values were obtained by scanning the ECDL past the 777.2 nm atomic oxygen transition at 0.5 kHz. Data were acquired simultaneously at four different channels (1 MHz per channel) for each individual optical line-of-sight during the full course of a run. A moving-average of 500 successive scans was performed to reduce baseline distortion noise caused by significant steering of laser light directed across the column of hot gas (i.e. beamsteering noise). In the present study, temperature time histories are displayed for ports A, B, C, and D of the optical copper segment with 1 second measurement resolution.

A. First-Generation MLOS Sensor: September 2012 Measurement Campaign

The first successful MLOS experiments were conducted for IHF Test #251. The results presented in this section are for a low-enthalpy arcjet run (Run #002) with significant radial add-air injection. The arc heater settings for this particular run are presented in Table 4 below, where P_c is the chamber pressure, I_A is the applied arc current, V_A is the applied arc voltage, and $\dot{m}$ is the mass flow rate for different input gases:

Table 4. Arc Heater Settings: IHF Test #251.

Condition	Run #	P_C (atm)	I_A (A)	V_A (V)	$\dot{m}_{main-air}$ (g/s)	$\dot{m}_{add-air}$ (g/s)	$\dot{m}_{argon}$ (g/s)
I	**002**	2.29	1770	2360	80	340	31

Due to the relatively large amount of add-air injection and the low-enthalpy, low-pressure nature of Run #002, data collected at optical port D with its short pathlength and lower gas temperature at the edge of the plasma column produced an absorption SNR that was too low to yield a usable lineshape. Figures (16) and (17) show temperature time histories measured at the three remaining optical ports A, B, and C with longer pathlengths.

For this particular run, the total test time can be divided into three major periods: startup, steady, and shutdown. During the arc startup period (0s − 110s), after a quick temperature overshoot, cold add-air is injected to tailor the heater enthalpy to desired test condition **I**. Once this design condition is achieved, all facility input parameters (air/argon flow rates, and current) are held constant while TPS articles are being tested in the evacuated test cabin (110s − 950s). Lastly, once testing is finalized, arc shutdown is initiated (950s − 1100s). As the amount of input add-air decreases, the overall plenum temperature raises at all optical ports to a secondary plateau, where it remains constant for a short period of time before the arc is completely turned off.

During steady arcjet operation, the temperature measured at the centerline optical port B is higher than at ports A and C. Thus, the accelerated gas flow has a hotter core and colder outer region. This is expected for a variety of reasons such as magnetic field confinement of electron motions to the center-most region of the heater, heat transfer to the walls of the water-cooled copper segments, and mixing/penetration properties of radial add-air injection.

The laser sensor is capable of detecting both long (< 0.1Hz) and short (~1Hz) time-scale temperature fluctuations throughout the course of the run. Short time-scale fluctuations (i.e. temperature measurement noise) in ports A and C are more pronounced than in the centerline port B. Although this noise in temperature readout could be interpreted as incomplete mixing of cold add-air with hot arc-heated gas, it is more likely due to weak line-of-sight absorbance coupled with significant beamsteering noise which affected baseline fitting and increased measurement error. Further investigation into beamsteering noise reduction was required to improve overall SNR and properly assess the add-air mixing process.

Long time-scale fluctuations were also observed. Although the temperatures at the symmetric ports A and C are nearly equal, a periodic discrepancy between measurements in these two ports serves as an indication that the thermal profile of the plasma is unsteady, and assumptions of an axisymmetric flow may not always hold throughout the test period. These long time-scale fluctuations seem unrelated to add-air injection since input flow rates were maintained constant during steady arcjet operation. Rather, they were more likely caused by the arc-foot rotation due to current-induced magnetic fields in the heater, to prevent electrode erosion. Experiments at other arcjet operating conditions were needed in order to validate this prediction.
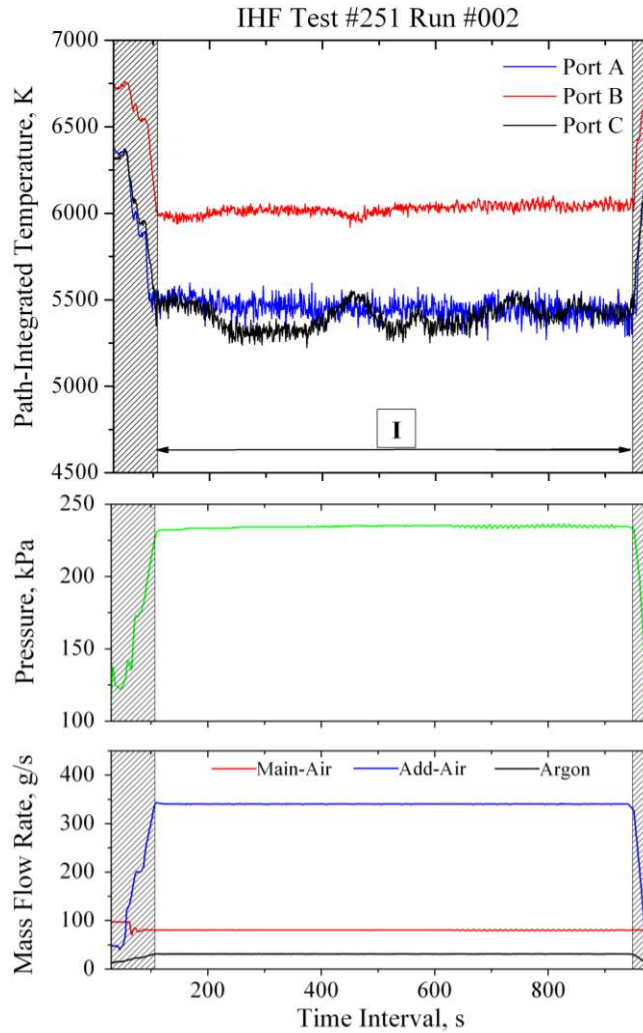
Figure 16. Path-integrated temperature measurements and facility data for IHF Test #251 Run #002.
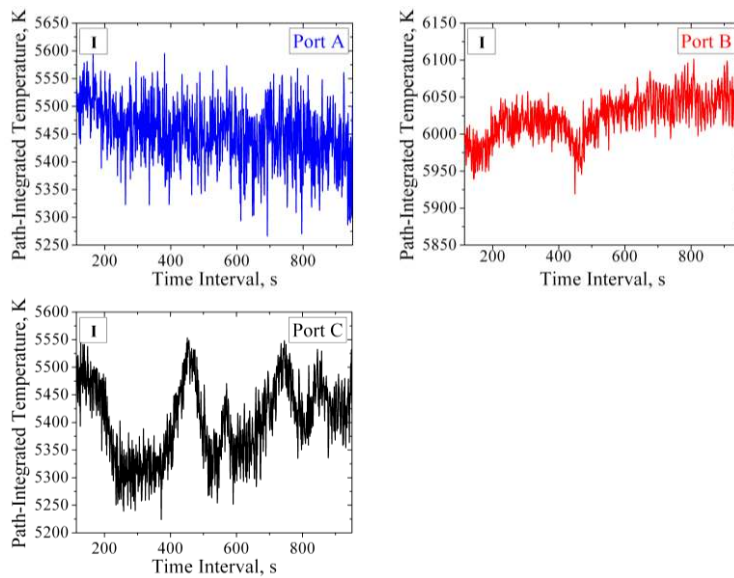

Figure 17. Detailed temperature time history for condition I at optical ports A, B, and C.

13
American Institute of Aeronautics and Astronautics

B. Beamsteering noise reduction efforts

Improvement of sensor performance in order to more accurately evaluate nonuniformities in the arc heater relied on suppression of beamsteering noise which limited the sensor's detectivity range due to low SNR. The add-air injection occurs just upstream of the TDL measurements, inducing high-frequency noise (~30 kHz) and distorting absorption lineshapes. Although data averaging helps reduce random distortions, errors in integrated absorbance area obtained by fitting distorted profiles propagate as errors in measured temperature.

In graded-index multimode-fibers, modal dispersion occurs due to fiber imperfections, where higher-order modes traveling near the edges of the fiber core are delayed with respect to low-order modes traveling near the center of the core upon arriving at the fiber exit and light power carried by each of these modes will be out of phase. Depending on how the plasma steered light is coupled into the multi-mode fiber, and on how the fiber modes are excited, the output power profile will change, and the measured transmitted signal will fluctuate.

To address this problem, the catch optics system was modified to house a doublet lens mount which focused divergent laser light exiting the multi-mode fiber fully on the detector chip's surface. The new light collection system successfully reduced signal fluctuations caused by out-of-phase modes within the fiber and significantly improved SNR. Figures (18) and (19) show measured transmission and absorption signals for a catch optics system with and without a doublet lens mount, respectively.
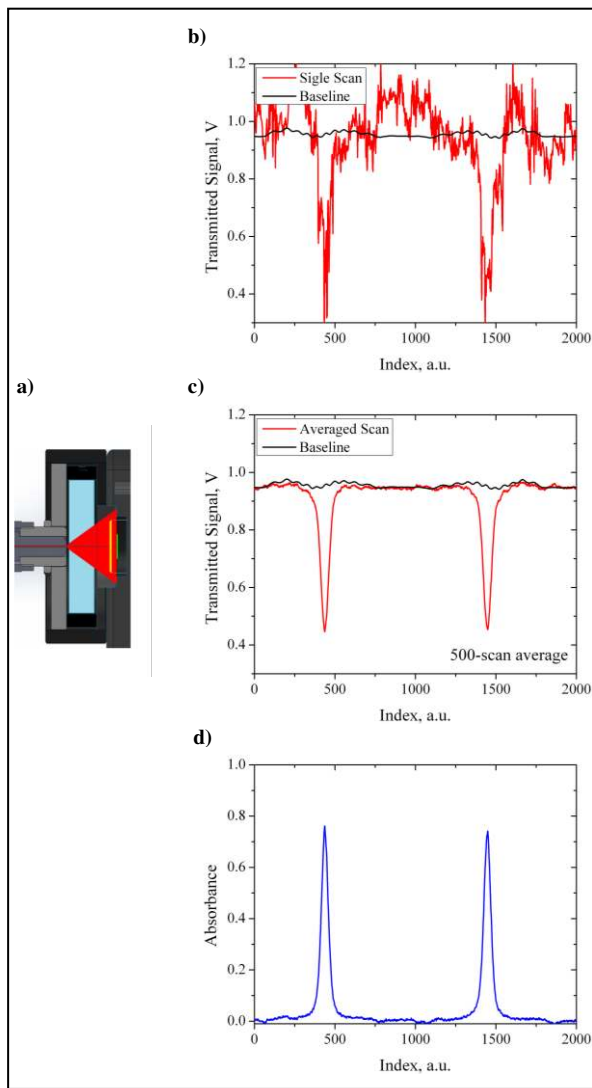

Figure 18. a) Original catch system without doublet lens mount. b) Example single scan transmission data. c) Example averaged scan transmission data. d) Example measured absorption profile with significant distortions due to poor baseline fitting.
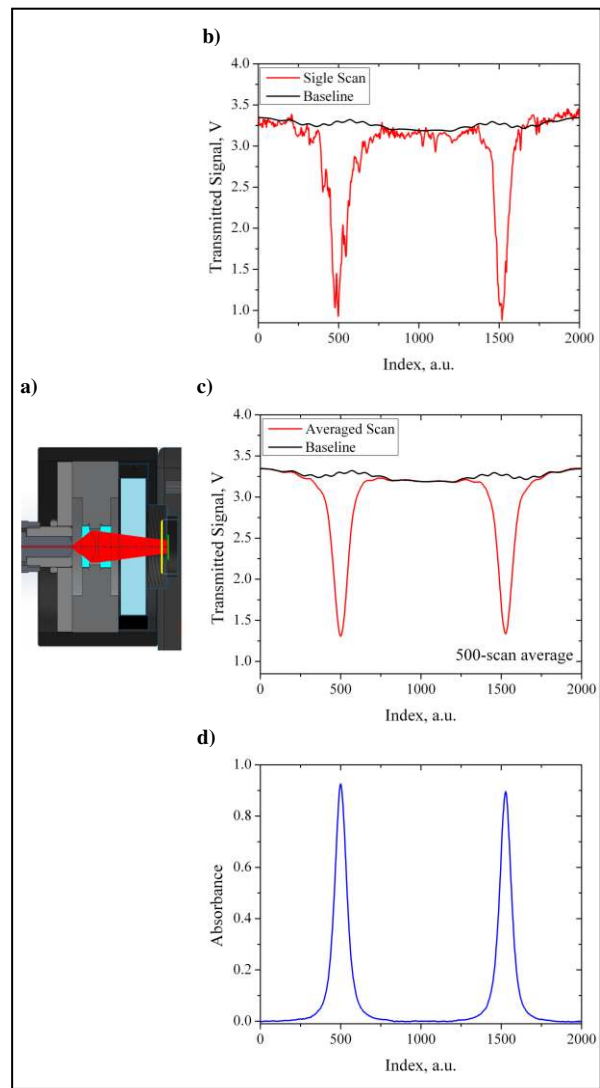
Figure 19. a) Modified catch system with doublet lens mount. b) Example single scan transmission data. c) Example averaged scan transmission data. d) Example measured absorption profile free of baseline-fitting distortions.

C. Second-Generation MLOS Sensor: March 2012 Measurement Campaign

Experiments were conducted to further investigate sensor operation for different arcjet operating conditions using the modified catch optics system. MLOS data were acquired during IHF Test #1313 for two different arcjet runs (Run #014 and Run #013). The heater settings for each run are shown in Table 5.

Table 5. Arc Heater Settings: IHF Test #1313

Condition	Run #	P_C (atm)	I_A (A)	V_A (V)	$\dot{m}_{main-air}$ (g/s)	$\dot{m}_{add-air}$ (g/s)	$\dot{m}_{argon}$ (g/s)
II	014	2.22	2000	3680	200	55	25
III	013	4.75	3500	4300	270	330	42
IV	013	5.95	3500	6050	545	55	42

Run #014 was a low-enthalpy, low-pressure run at slightly higher arcjet power than Run #002 and minimal add-air injection. Improved sensor SNR allowed for temperature measurements at all four optical ports, although absorbance levels in port D were still significantly low with less than 1% peak absorbance. Measured temperature time history for this particular run is shown in Fig. (20). Run #014 was a relatively short run (~6 min), and no evidence of temporal fluctuations was observed. Figure (21) expands the temperature scale to evaluate the temperature stability. At the centerline of the plasma, column temperature fluctuations are of the order of 0.14% . However, despite the steady thermal profile, a substantial difference in measured absorbance between symmetric ports A and C indicates that the flow is not axisymmetric during the course of the run, and spatial nonuniformities exist within the plasma. The thermal profile appears to be slightly skewed from an axisymmetric distribution, with higher gas temperatures measured below the centerline port B than above.

The laser sensor detected similar temperature asymmetry during Run #013, for both high (**III**) and low (**IV**) add-air conditions, as shown in Fig. (22). These are the first successful MLOS measurements at IHF plenum at high pressure conditions (~6 atm) using TDLAS. These results indicate that although add-air injection increases the overall temperature gradient across the plasma column as expected, it is not the driving mechanism for the temperature asymmetry, as the difference is consistent regardless of the amount of cold air input. However, the significantly large variations in measured temperature at port D for the high-add air condition **III**, compared to the low add-air case **IV** can be interpreted as incomplete mixing between the cold and hot gases near the walls of the copper segment. The injection of add-air, however, does not seem to induce short time-scale fluctuations in temperature at the core, as the variations in measured temperature in port A, B, and C remain fairly constant.

A plausible explanation for similar asymmetric footprint in Run #014 and Run #013 may be that the same electrode package assembly was used, which may influence how the electrical arc physically attaches itself between the electrodes. If the plasma peak temperature shifts to an off-center position due to displacement of the arc-attachment, the thermal profile could appear skewed and the measured temperatures across the symmetric optical ports A and C could differ. Another possible explanation for the observed asymmetry might be that nonuniform radial injection of gas produced a profile not centered at the constrictor bore.

Results from a nozzle sweep at the test cabin using a nullpoint calorimeter probe during Run #014 are consistent with the results of laser absorption experiments, where the enthalpy profile was found to be shifted towards the bottom half. While the enthalpy profile measured with the calorimeter was reasonably symmetric, a small level of asymmetry can be observed in Fig. (25a). The calorimeter sweep followed a 45 degree angle line path across the nozzle exit cross-section, from the lower east corner of the IHF, to the upper west corner of the facility as illustrated in Fig. (25b). The probe measured a hotter flow below the centerline location on the negative side of the sweep, which is in agreement with the higher laser light absorption measured at port C compared with port A in the plasma plenum for Run #014; the stratified temperature in the heater column could persist in the expansion and account for the asymmetry in the heat flux. Overall, these results demonstrate the measurement capability of the laser sensor to accurately monitor temporal and spatial nonuniformities in the plenum of the IHF arcjet during the course of a run.
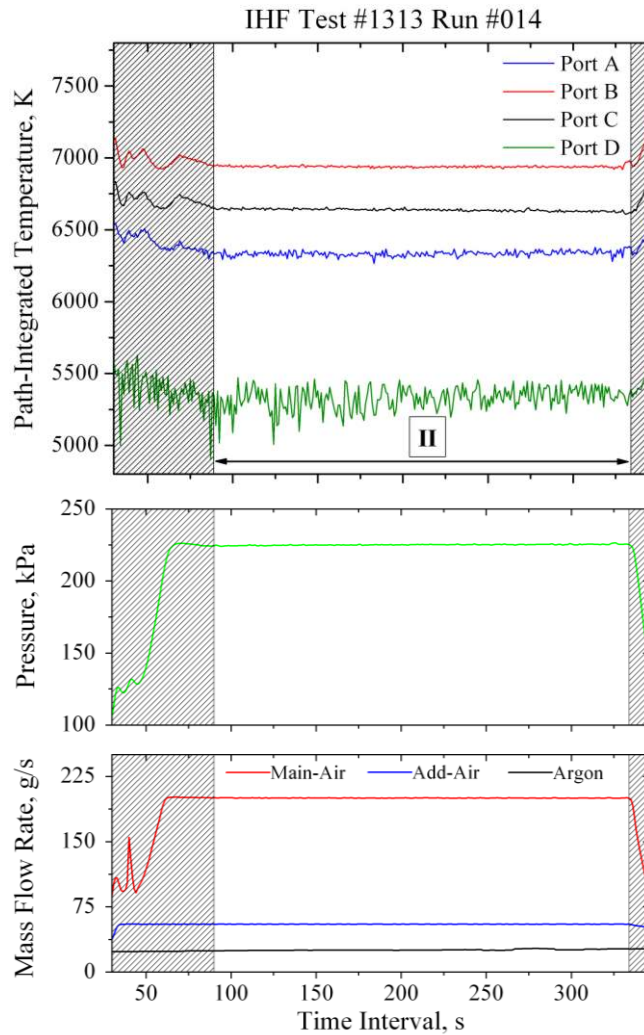
Figure 20. Path-integrated temperature measurements and facility data for IHF Test #1313 Run #014.
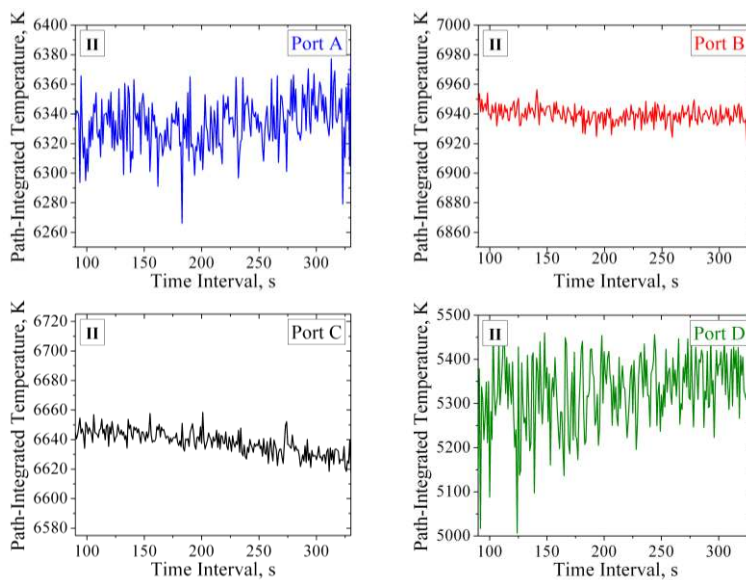

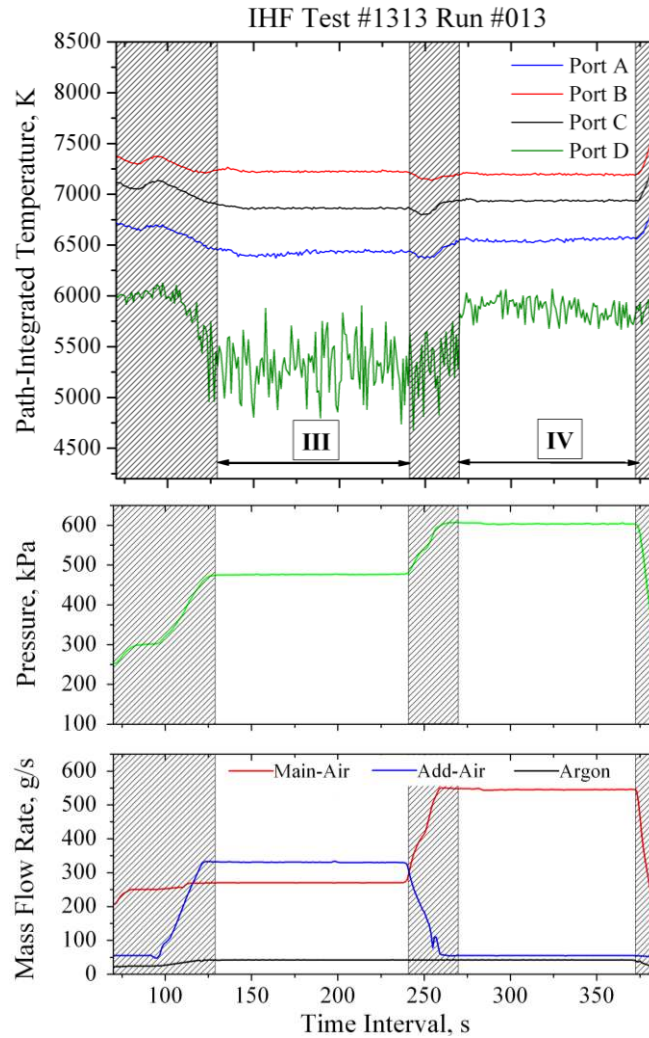**Figure 21. Detailed temperature time history for condition II at optical ports A, B, C, and D.**

American Institute of Aeronautics and Astronautics

Figure 22. Path-integrated temperature measurements and facility data for IHF Test #1313 Run #013.
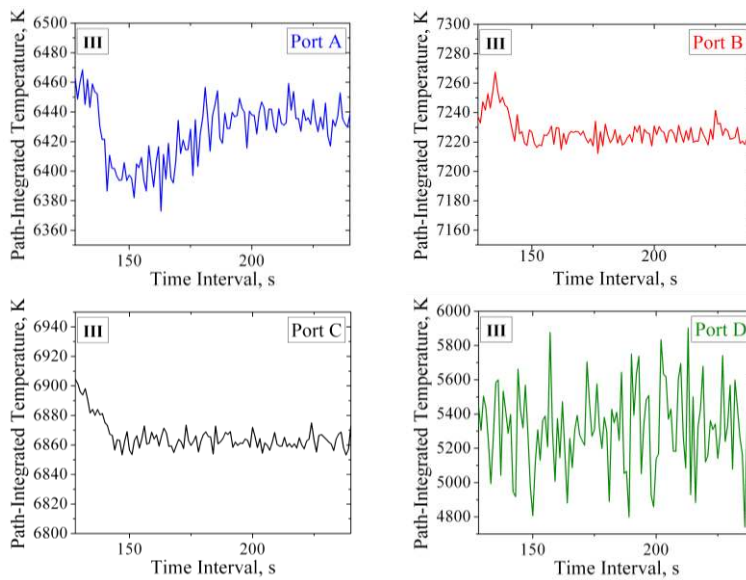
Figure 23. Detailed temperature time history for condition III at optical ports A, B, C, and D.

17
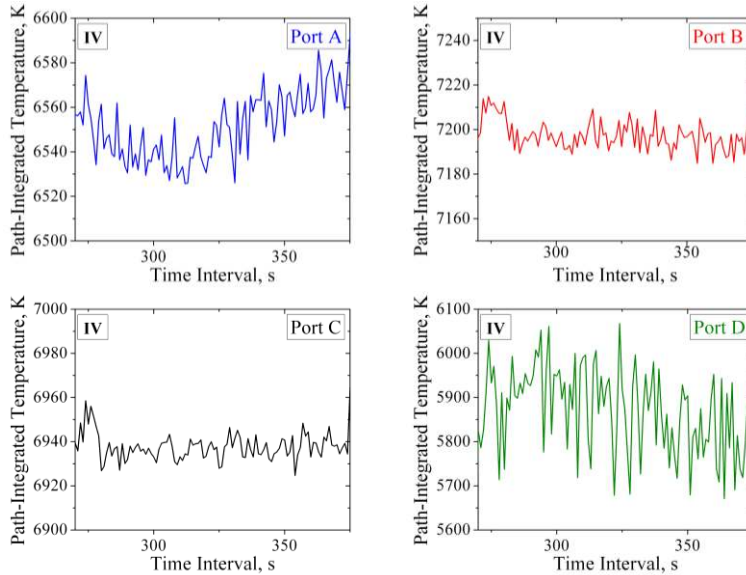American Institute of Aeronautics and Astronautics

Figure 24. Detailed temperature time history for condition IV at optical ports A, B, C, and D.
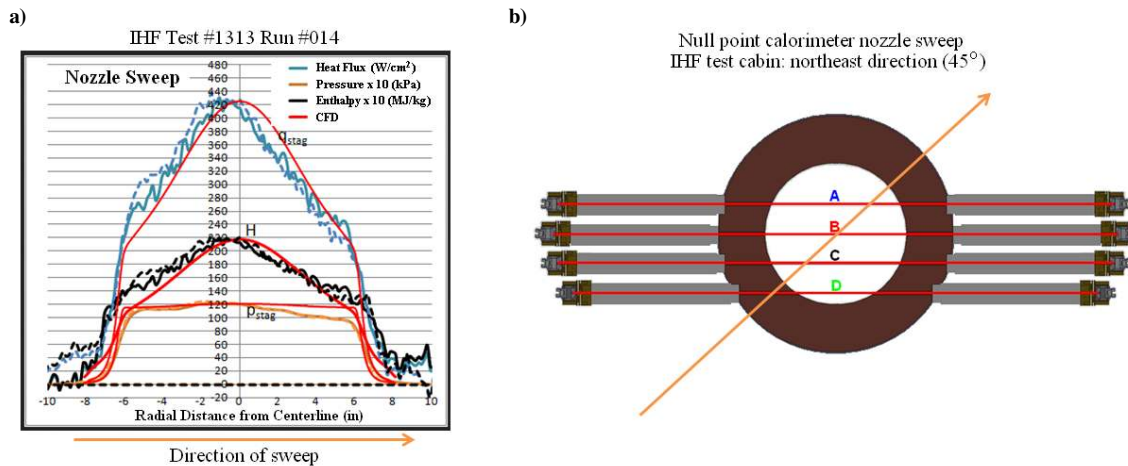

Figure 25.   a) Nullpoint calorimeter nozzle sweep for Test #1313 Run #014, showing a slightly skewed enthalpy profile, in close agreement with TDL measurements in the arc heater. b) Illustrative schematic showing the direction of the nullpoint calorimeter sweep at the test cabin (see Fig. 9) with respect to the optical disk located at the nozzle inlet.

D. Comparison of simulated and measured path-integrated temperatures in the IHF arc heater

Temperature profiles in the plenum are computed using NASA's in-house computational fluid dynamics (CFD) code *DPLR*[18] based on distributions of measured enthalpy in the nozzle exit from sweeps of nullpoint calorimeters across the free jet. Details on the exact procedure for computing these flow fields in the plenum are described by Prabhu et al.[18] Simulated path-averaged temperatures can be calculated directly from temperature and species axial distributions obtained from CFD for comparison with TDL measurements. Figure (26) illustrates the simulated symmetric radial profile of temperature and flow species in the plenum for Run #014. In order to compute the path-integrated absorbance at each LOS, the plasma is divided into 100 concentric rings in which the thermodynamic properties may be assumed constant and the plasma at each discretized location is assumed to be in local thermodynamic equilibrium. A path-integrated absorbance profile is then obtained by adding the contributions of each discrete ring along the optical pathlength of each line-of-sight. Simulated and measured path-averaged absorbance profiles are shown in Fig. (27) below for comparison. The measured absorbance on port D nearly matches the CFD, and port A is in good agreement. However the CFD profile seems to under-predict the centerline temperature, as the measured absorbance in port B is larger than the CFD absorbance. The integrated areas are obtained by fitting each aggregated absorbance profile with a Voigt lineshape and CFD path-averaged temperatures

18

American Institute of Aeronautics and Astronautics

are calculated for each LOS. Figure (28) shows both the simulated and measured path-integrated temperatures, where TDL data seem in relatively good agreement with predicted CFD thermal profile, except for the asymmetric temperature distribution measured experimentally and the under-predicted CFD centerline temperature (~350 K, 5 %). The CFD framework makes use of an underlying assumption that the flow is adiabatic (i.e. lossless) in the inviscid core flow between the plenum and the test cabin and the discrepancy between experimental and theoretical results could be related to the non-adiabatic nature of the flow in the nozzle. Future examination of TDL measurements and CFD solutions for various arcjet operating conditions will help improve our understanding of uncertainties due to non-ideal processes and aid the development of enhanced models for arc-heated air plasma flows expanded through convergent-divergent nozzles.
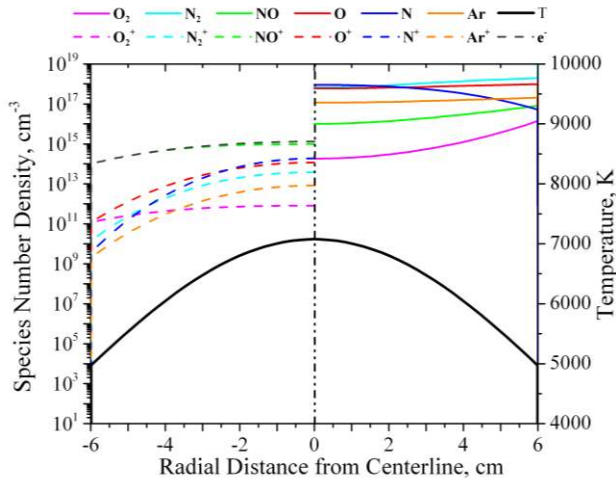

Figure 26. Simulated profile of temperature and species number density in the arc heater for IHF Test #1313 Run #014.
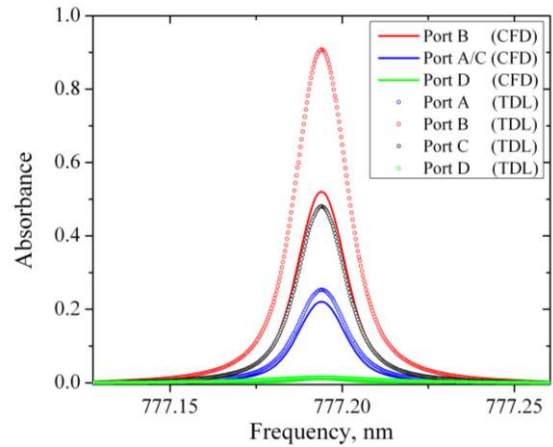

Figure 27. Measured (TDL) and simulated (CFD) path-averaged absorbance profiles for IHF Test #1313 Run #014.
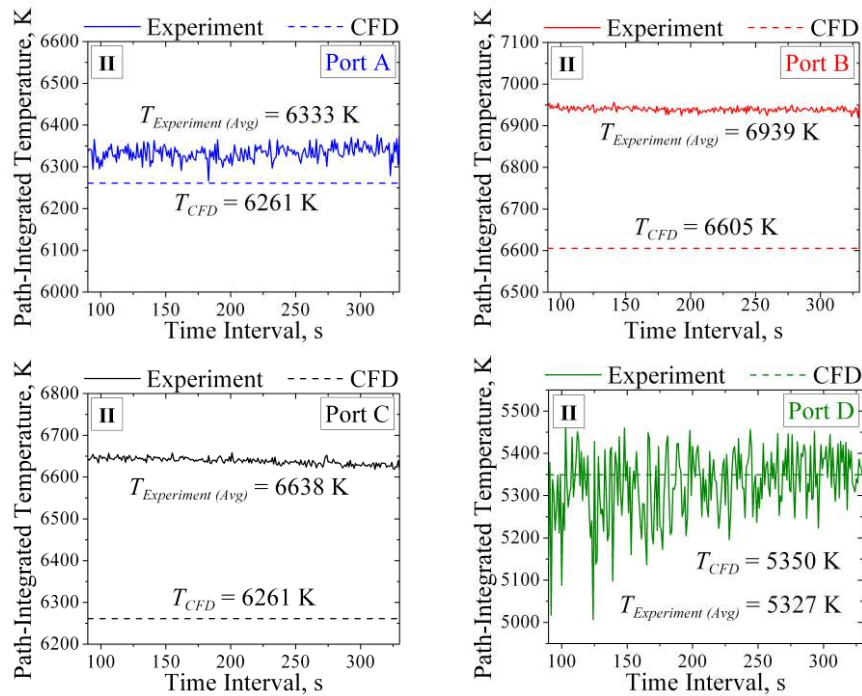

Figure 28. Measured and simulated path-integrated temperatures at optical ports A, B, C and D for IHF Test #1313 Run #014.

V. Conclusion

In the present work, an external cavity diode laser sensor was developed for *in situ*, simultaneous measurements of arc-heated gas temperature at multiple lines-of-sight to probe the arc-heated gases in the plenum and monitor fluctuations. Experiments confirmed the TDL sensor's capability of making precise measurements of flow properties at several arcjet operating conditions, including low and high add-air injection as well as different pressure regimes. This work provides experimental evidence that for high add-air input conditions, the flow mixing near the walls of the heater may not be fully complete upon entering the nozzle inlet. Also, long time-scale fluctuations were carefully monitored, and are believed to be caused by the periodic displacement of the arc-attachment due to current-induced magnetic fields in the heater. Moreover, TDL measurements and CFD solutions of the thermal profile in the heater show relatively good agreement, although the CFD provides a symmetric solution and the sensor finds a significant temperature asymmetry for some arc heater conditions/assembly.   Future analysis for a variety of arcjet operating conditions will help improve/anchor existing models that predict the thermal profile of arc-heated flows in the heater of the IHF.

Acknowledgments

References

[1]Glass, David E. "Ceramic matrix composite (CMC) thermal protection systems (TPS) and hot structures for hypersonic vehicles." AIAA-2008-2682, *15th AIAA Space Planes and Hypersonic Systems and Technologies Conference, Dayton*. Vol. 28. 2008.

[2]Laub, B., Venkatapathy, E., "Thermal protection system technology and facility needs for demanding future planetary missions." *Planetary Probe Atmospheric Entry and Descent Trajectory Analysis and Science*. Vol. 544. 2004.

[3]Smith, R. K., D. A. Wagner, and James Cunningham. "A survey of current and future plasma arc-heated test facilities for aerospace and commercial applications." AIAA-1998-0146. *36th AIAA Aerospace Sciences Meeting and Exhibit*, 1998.

[4]Kim, S., Jeffries, J. B., Hanson, R. K., Raiche, G. A., "Gas Temperature in the Arc-heater of a Large Scale Arcjet Facility using Tunable Diode Laser Absorption," AIAA. 2005-900. *43rd Aerospace Sciences Meeting*, 2005.

[5]Winter, M W, Prabhu, D K, Taunk, J S, and Terrazas-Salinas, I, "Emission Spectroscopic Measurements in the Plenum of the NASA IHF Arc Jet Facility," AIAA-2010-4522, *10th AIAA/ASME Joint Thermophysics and Heat Transfer Conference*, 2010.

[6]Ralchenko, Yu., Kramida, A.E., Reader, J., and NIST ASD Team (2011). NIST Atomic Spectra Database (ver. 4.1.0), [Online]. Available: http://physics.nist.gov/asd3 [2011, August 24]. National Institute of Standards and Technology, Gaithersburg, MD.

[7]Hanson, R. K., and Jeffries, J. B., "Diode laser sensors for ground testing." AIAA-2006-3441. *25th AIAA Aerodynamic Measurement Technology and Ground Testing Conference*, Vol. 2, 2006.

[8]Hanson, R. K., "Applications of quantitative laser sensors to kinetics, propulsion and practical energy systems." *Proceedings of the Combustion Institute,* Vol. 33 No.1, 2011, pp. 1-40.

[9]Colonna, G., and Capitelli, M. "A few level approach for the electronic partition function of atomic systems." *Spectrochimica Acta Part B: Atomic Spectroscopy*. Vol. 64 No. 9, 2009, pp. 863-873.

[10]Kim, S., "Development of Tunable Diode Laser Absorption Sensors for a Large-Scale Arc-Heated-Plasma Wind Tunnel," Ph.D. Dissertation, Mechanical Engineering Dept., Stanford University, Stanford, CA, 2004.

[11]Gordon, S., and McBride, B. J., "Computer program for calculation of complex chemical equilibrium compositions and applications," National Aeronautics and Space Administration, Office of Management, Scientific and Technical Information Program, 1996.

[12]Baer, D. S., Chang, H. A., and Hanson, R. K., "Semiconductor laser absorption diagnostics of atomic oxygen in an atmospheric-pressure plasma." *Journal of Quantitative Spectroscopy and Radiative Transfer.* Vol. 50 No. 6, 1993, pp. 621-633.

[13]Griem, H.R., *Plasma Spectroscopy,* McGraw-Hill, New York, NY, 1964.

[14]Laux, C., "Optical diagnostics and radiative emission of air plasma," Ph.D. Dissertation, Mechanical Engineering Dept., Stanford University, Stanford, CA, 1993.

[15]Wiese, W. L., *Plasma Diagnostics Techniques*, Academic Press, New York, NY, 1974.

[16]Griem, H.R., *Spectral Line Broadening by Plasmas,* Academic Press, New York, NY, 1974.

[17]Humlicek, J., "Optimized computation of the Voigt and complex probability functions." *J. Quant. Spectrosc. Radiat. Transfer,* Vol.27, 1982, pp. 437-444.

[18]Prabhu, D. K., Saunders, D. S., Oishi, T., Skokova, K., Santos, J., Fu, J., Terrazas-Salinas, I., Carballo, E., and Driver, D. M., "CFD Analysis Framework for Arc-Heated Flowfields, I: Stagnation Testing in Arc-jets at NASA ARC," AIAA-2009-4080, *41st Thermophysics Conference*, 2009.